SIMULATION AND EXPERIMENTAL INVESTIGATION OF A COMBINED CONTROL METHOD FOR STRAY GRAIN DURING SINGLE CRYSTAL BLADE SOLIDIFICATION

Haoyu Zhao, Kun Bu, Binqiang Wang and Sheng Mou
Key Laboratory of High Performance Manufacturing for Aero Engine, Ministry of Industry and Information Technology, School of Mechanical Engineering, Northwestern Polytechnical University, Xi'an 710072, Shannxi, People's Republic of China

Pengguo Duan
Avic Xi'an Aero-Engine (Group) Ltd., Xi'an 710100, People's Republic of China

https://doi.org/10.1007/s40962-024-01357-x

Abstract

It is of great significance to effectively prevent the stray grain defect at the edge plate of nickel-based superalloy single crystal blades. In this study, the evolution of the mushy zone and the growth of grain adjacent to the edge plate was first simulated by the temperature field and cellular automaton-finite element (CAFE) model, combined with a single crystal blade solidification experiment; it was proved that modifying the withdrawal rate alone was insufficient to prevent the stray grain formation. Then, the formation reason of the heat barrier zone and the irregular distribution pattern of the mold shell thickness were revealed by quantifying the present mold shell thickness near the edge plate through an industrial conical beam computed tomography. Based on these results, a combined control method for stray grain was proposed, which involves the use of precise measures such as non-uniform mold design, exact addition of process bars, and variable withdrawal rate. Simulation analysis demonstrated that this method can substantially reduce the undercooling range and average undercooling at the edge plate by 45.5% and 31.6%, respectively, and then eliminate the isolated undercooling zone. The macrostructure and microstructure of the blade cast by this method verified the effectiveness in inhibiting stray grain, and it will be a promising approach to manufacturing single crystal blades.

Keywords: *single crystal superalloy, stray grain formation, temperature field, process bars, non-uniform shell thickness*

Introduction

Single crystal (SX) blades exhibit superior creep resistance, high-temperature impact resistance, and durability compared to the equated and columnar crystal, which have been extensively utilized in aero engines and industrial gas turbines.[1,2] Bridgman directional solidification combined with an investment casting process is adopted to manufacture SX blades.[3] Stray grain is a typical defect particularly common at the edge plate during the SX blade production.[4] Since the blade becomes susceptible to crack or even fracture along the grain boundaries of these newly formed grains under the high-temperature and pressure impact load. So, effectively controlling the generation of stray grain has become an urgent issue in scientific research and industrial production.

Previous studies have shown that the formation of stray grain is mainly due to the concave isotherm during directional solidification, resulting in the edge plate reaching the critical nucleation undercooling before the primary dendrite grows into this position.[5] Generally, the formation of stray grain is mainly affected by process parameters, the composition of the superalloy, the cooling rate, the structure of the edge plate, and other factors.[6,7] Until now, several methods have been proposed to prevent the formation of stray grain. Ren et al.[8] proposed a real-time

Received: 01 March 2024 / Accepted: 15 April 2024
Published online: 11 May 2024

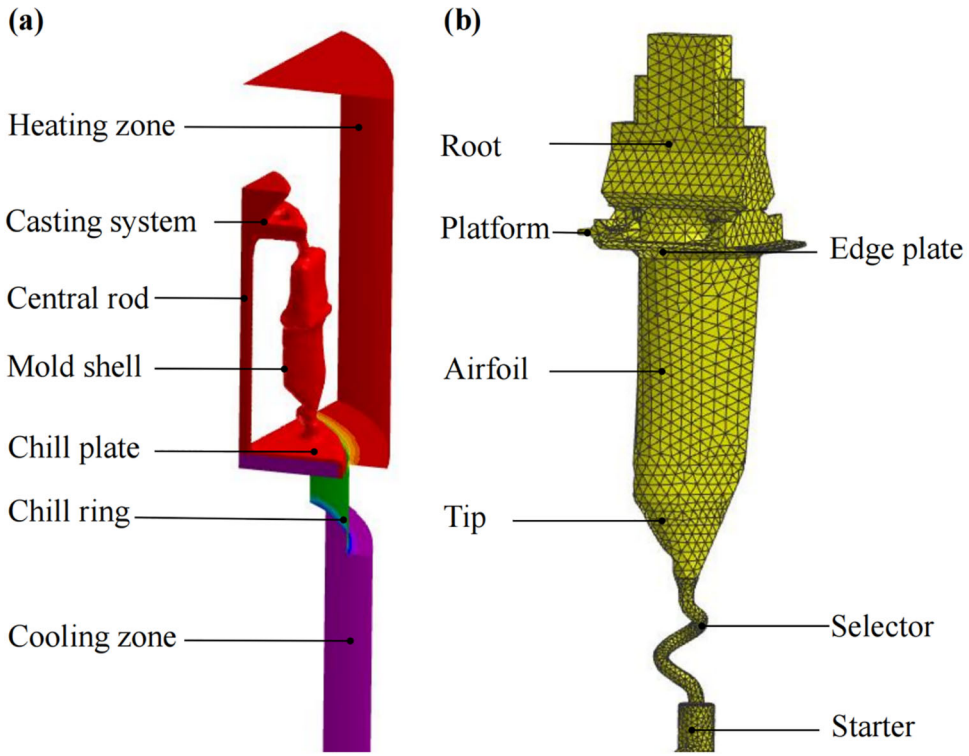

Figure 1. Diagram of the physical model, (a) Bridgman directional solidification furnace and the computational domain; and (b) the mesh of the SX blade.

Table 1. Nominal Chemical Composition of Single Crystal Superalloy DD6

Element	Ni	Nb	Cr	Co	W	Mo	Al	Hf	Ta	Re
wt%	Bal	0.6	4.3	9	8	2	5.7	0.1	7.3	2

Table 2. Properties of Mold Shell and Ceramic Core Material

Material	Density (kg/m^3)	Conductivity (W/m/K)	Specific heat (kJ/kg/K)
Al_2O_3	3800	22	0.78
Ceramic core	1520	0.65	1.10

adjustment of the withdrawal rate method to fabricate blades with complex geometry. Qin et al.[9] proposed a non-uniform thickness mold design to increase temperature gradient and straighten the solid/liquid interface shape in directionally solidified superalloy blades, contributing to reducing or eliminating the freckle and stray grain defects; unfortunately, the effectiveness of this method was not verified with actual SX blade. Szeliga et al.[10] selected an appropriate position for the internal heat baffle relative to the platform according to the measured and predicted temperature distribution and obtained a convex or nearly flat shape of the solid/liquid interface. Ma[11] addressed the poor heat dissipation condition of the heat barrier zone between the edge plate and the blade body by using the heat conductor technique, resulting in the maximum undercooling at the edge plate being significantly reduced, and then, stray grain could be effectively inhibition. However, the addition of internal heat baffle and graphite heat conductor obviously increases the process complexity and risk of mold shell cracking, respectively. Meyer et al.[12] developed a grain continuator method to pre-implant the primary SX into the area where the stray grain will form at the edge plate, and Qiu et al.[13] determined the position of process bar addition based on the cooling rate, but inappropriate process parameters may introduce low angle grain boundaries. Based on a comprehensive literature review, it was found that the current control of stray grain mainly adopted a single method of adjusting process parameters or auxiliary structures. However, previous attempts to eliminate stray grain by reducing the withdrawal rate have been proven insufficient, and the specific position for the process bar addition remains unclear.

In this paper, a novel combined control method for stray grain was proposed, which utilized fixed-point adding of process bars, non-uniform mold design, and variable withdrawal rate to improve the undercooling and overheating state of the edge plate. The add position of process bars was determined by the appearance site of stray grain in the un-optimized process. The design of non-uniform mold thickness and variable withdrawal rate was according to the

Table 3. Nucleation Parameters Used for Grain Structure Simulation

Nucleation kinetics	ΔT_{max}	$\Delta T\sigma$	n_{max}
Surface nucleation	2 °C	1 °C	1.65×0^{10} m^{-2}
Volume nucleation	20 °C	2 °C	9×0^{9} m^{-3}

simulation results. Then, the effectiveness of this method was verified in the process of directional solidification of stray grain-free SX blades.

Simulation and Experimental Details

Physical Model

In this work, the Bridgman directional solidification method was used to fabricate the SX blade. Figure 1a presents the structure of the furnace and the computational domain. The computational domain is one-half of the apparatus (the excess volumes of the casting system and chill plate were subtracted for a clearer view) and divided into 113,356 trihedrons control volumes, including the heating zone, casting system, central rod, mold shell, chill plate, chill ring, and cooling zone. Figure 1b shows the mesh of the blade, which consists of a starter, selector, tip, airfoil, platform, edge plate, and root.

The temperature of the chill plate, melt pouring, mold preheating, and calculated termination are set as 25 °C, 1500 °C, 1550 °C, and 300 °C, respectively.[14] To achieve an accurate thermal field, it is important to account for the heat transfer coefficient between the mold shell and test specimen.[15,16] The interface heat transfer coefficient (HTCS) between the casting and the mold shell, as well as between the casting and the chill plate, was derived from the actual temperature data recorded during solidification. Subsequently, these coefficients were calculated using the inverse module within the commercial process modeling software, ProCAST. Further information can be found in Mou et al.[17] The emissivity of the surface of the mold shell, heating zone, and cooling zone is set as 0.85, 0.9, and 0.5, respectively. The chemical composition of the single crystal superalloy DD6 used for the simulation is listed in Table 1. The main component of the mold shell material is alumina,[18] with an initial thickness set to 7mm. And ceramic core was considered to be a rigid body. Their details of the mechanical and thermophysical parameters referenced from Qiu et al.[19] and Guo et al.[20] are presented in Table 2. A personal computer with AMD Ryzen 95,950×16-Core Processor3.40 GHz CPU and 16.0 GB RAM was used as the computing platform. It took approximately 35 hours to complete the numerical simulation by 16-core parallel computing.

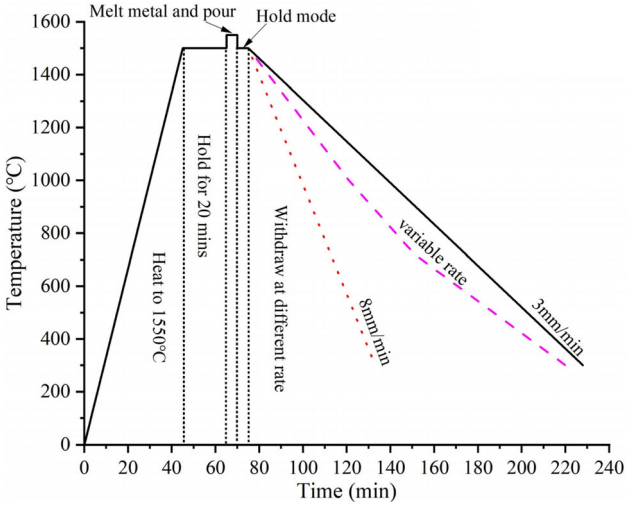

Figure 2. Investment casting heating cycle.

Heat Transfer Model

There are two types of heat transfer models in the directional solidification of the SX blade process. One is heat conduction, which transfers between the same or different materials in contact with each other. Another is heat radiation, which transfers in the interface between the mold shell and the heating zone or cooling zone of the furnace, solidified blade, and mold shell.[5]

According to the law of energy conservation, the heat transfer equilibrium equation can be expressed as follows:

$$\rho c\partial T/\partial t = \lambda(\partial^2 T/\partial x^2 + \partial^2 T/\partial y^2 + \partial^2 T/\partial z^2) + \rho L_f \partial f_s/\partial t + Q_R \quad \text{Eqn. 1}$$

where ρ is the fluid density, kg/m^3; c is specific heat capacity, kJ/(kg K); T is temperature, K; t is the time, s; λ is the thermal conductivity, W/(m K); L_f is the latent heat, kJ/kg; fs is the solid fraction; Q_R is the thermal radiation quantity, W/m^2; x, y, z are the coordinate.

Thermal radiation quantity Q_R is derived according to the law of Stefan–Boltzmann, which can be formulated as follows:

$$Q_R = \varepsilon\sigma(T_s^4 - T_{sur}^4) \quad \text{Eqn. 2}$$

where ε is the emissivity; σ is Stefan–Boltzmann constant, $\sigma = 5.67 \times 10^{-8}$ W/(m^2 K^4); T_s is the surface thermodynamic temperature, K; T_{sur} is the ambient temperature, K.

Nucleation and dendrite growth model

(1) Nucleation model

The mesoscale CAFÉ model was used to simulate the evolution of solidified grain structure after the macroscopic

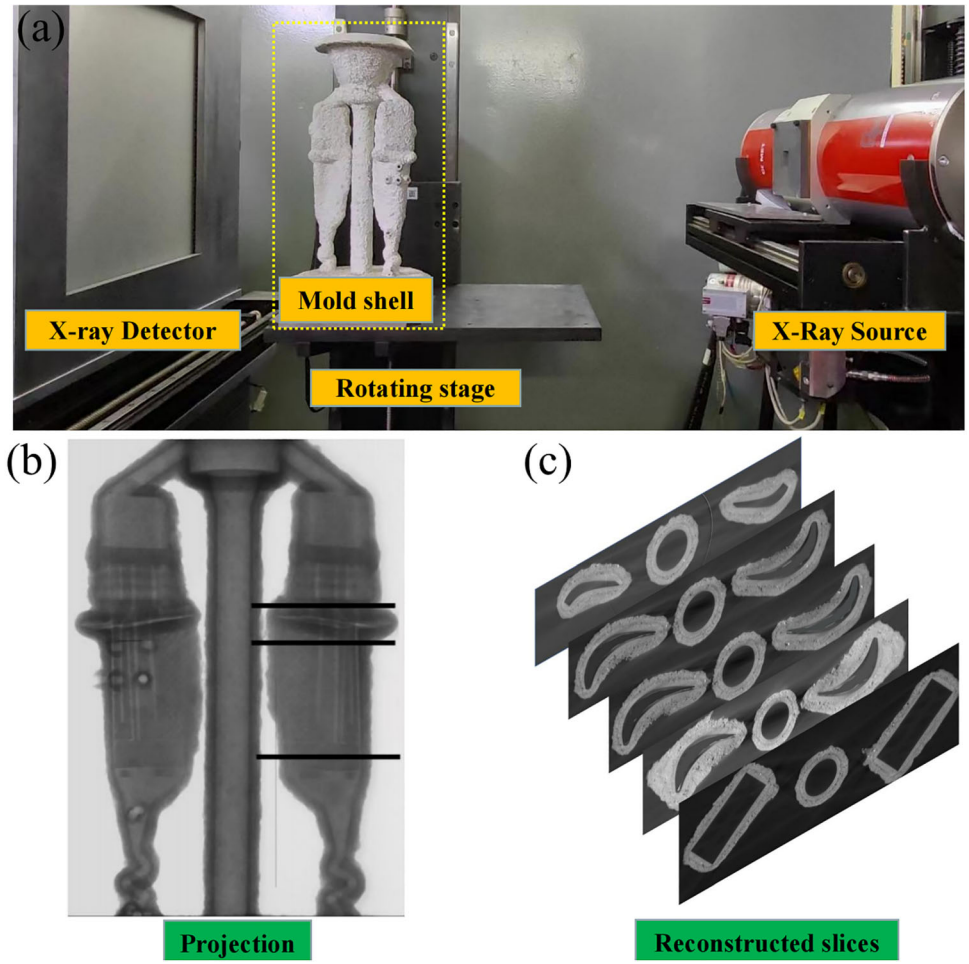

Figure 3. CT measurement of the mold shell.

temperature field was calculated by the macro-scale section of the commercial modeling code.[21] In the directional solidification of the SX blade process, the heterogeneous nucleation occurred at the surface of a chill plate or the edge plate position. A continuous nucleation distribution named Gaussian distribution was adopted to account for modeling the distribution of nucleation sites,[22,23] which can be described as follows:

$$n(\Delta T) = \frac{N_{\max}}{(2\pi)^{1/2}\Delta T_\sigma}\int_0^{\Delta T}\exp\left[-\frac{(\Delta T-\Delta T_{\max})^2}{2(\Delta T_\sigma)^2}\right]d(\Delta T) \quad \text{Eqn. 3}$$

where d_n is the increase in grain density, which is caused by an increase in the undercooling, $d(\Delta T)$. $\Delta T_{\max}$ is the maximum undercooling, ΔT_σ is the standard deviation, and $n_{\max}$ is the maximum density of nuclei obtained by the integral of the Gaussian distribution. Through the analysis of the parameters proposed by Kermanpur et al.[24], and Xia et al.[25], the optimal nucleation parameters were determined as shown in Table 3.

(2) Dendrite growth model

The relationship between the growth rate of the dendrite growth front and the undercooling can be simplified as a polynomial with coefficient:

$$V = a_2(\Delta T)^2 + a_3(\Delta T)^3 \quad \text{Eqn. 4}$$

where a_2 and a_3 are the constant valued as $3.35\text{x}10^{-7}$ m s^{-1} k^{-2} and $6.35\text{x}10^{-7}$ m s^{-1} k^{-3}, respectively, which is dependent on the composition of the DD6 alloy and given by Ren et al.[14] ΔT is the undercooling, and it was determined by the consideration of the multi-component extension to the Kurz, Giovanola, and Trivedi (KGT) model.[26]

Experimental Details

Single Crystal Directional Solidification Process

Mold shell work was conducted at Suzhou Gaojing New Materials Technology Co., Ltd. The prime coat was comprised of a zircon flour slurry and alumina powder, while the backup coat consists of alumina slurry and alumina powder. Each layer comprises one application of slurry followed by sand spraying. The shell comprises a total of

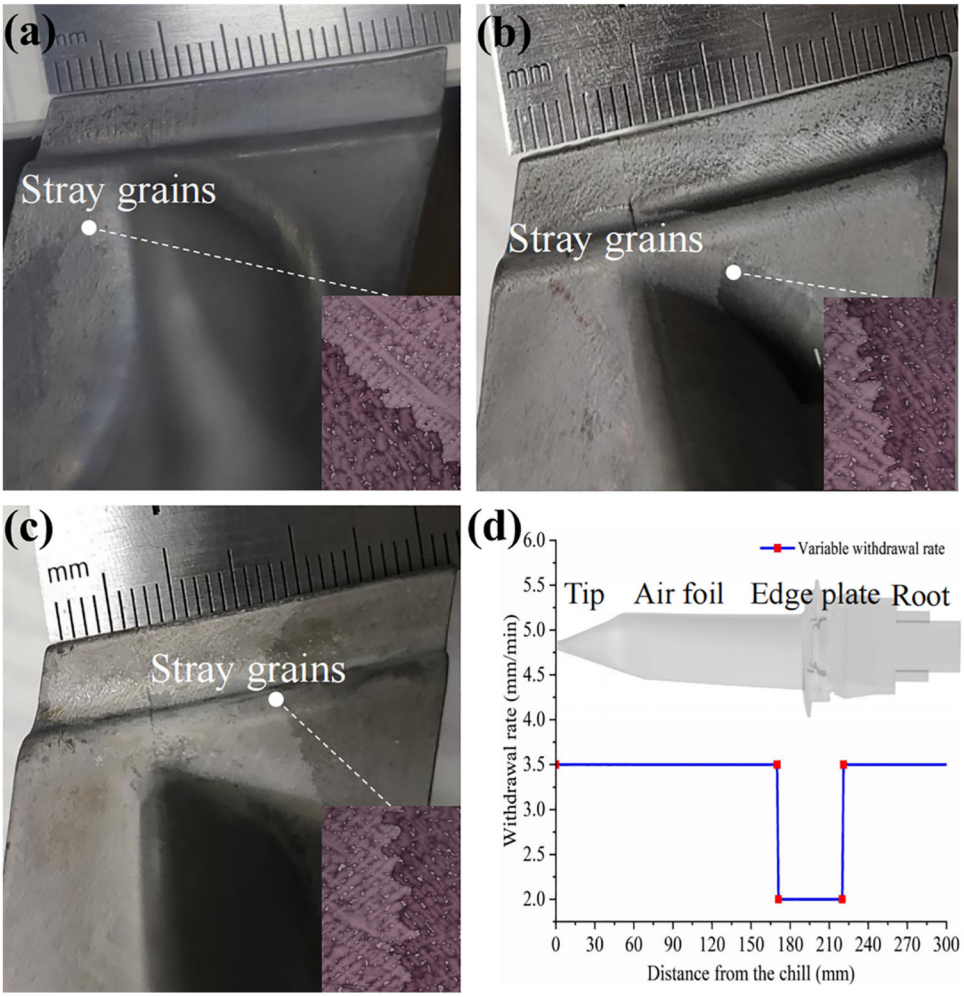

Figure 4. Macrostructure of the blades solidified under different withdrawal rates, (a) 3mm/min; (b) 8mm/min; (c) variable withdrawal rate; (d) the variable withdrawal rate curve. The insets are the microstructure pictures of the grain boundary indicated by the dotted white lines.

7.5 layers, with the final 0.5 layer being slurry only, without sand spraying. The overall thickness is approximately 7mm. Mixing is performed using a slurry barrel, and the mold shell thickness is adjusted manually by the number of slurry applications and shaping the shell. An industrial-scale investment casting facility at AECC Xi'an Aero Engineer Co., Ltd is utilized to produce the single crystal turbine blade, following standard procedures for mold preparation, including wax assembly, ceramic processing, and stem-autoclave dewaxing methods. The casting cycle is shown in Figure 2.

Microstructural Examination

Three blade samples were obtained in three cast experiments and labeled as A, B, and C, respectively. To check for stray grain formation, all samples were subjected to macroscopic corrosion by the etchant of H_2O_2:HC1 with a volume ratio of 1:9. Then, two slices above and below the edge plate were cut along the axial direction, and the dendrite structure was revealed by the standard metallographic techniques. The etchant of HNO_3: HF: $C_3H_8O_3$ with a volume ratio of 1:2:3 was used for this microscopic corrosion[27] and then, observed with a confocal laser microscope (Olympus OLS4000).

CT Detection

The thickness of the mold shell is easily distributed unevenly due to the layout, blade structure, and other reasons in the preparation process.[28] The slurry usually accumulates in the transition area between the blade body and the edge plate, resulting in the formation of the heat barrier zone.[6] Quantification and precise control of the thickness of this position are necessary to change the thermal condition. Hence, an industrial cone-beam computed tomography (CT) system with a voltage of 300KV, current of 1mA, and resolution of 100μm pixels was used to detect mold shell and reveal the distribution rule of mold shell thickness.[29]

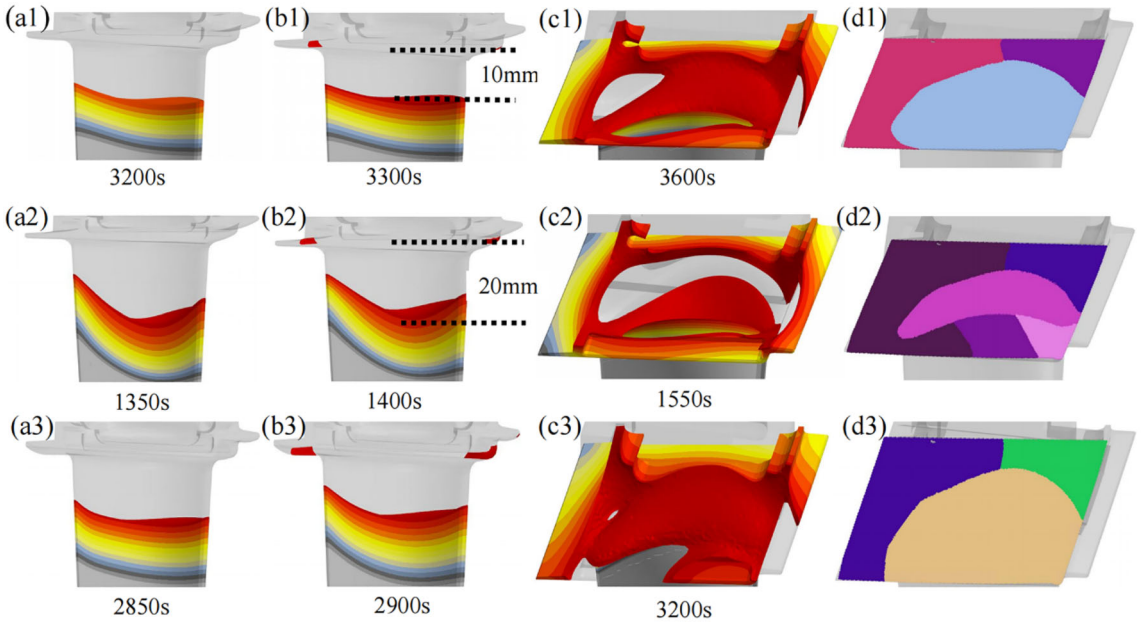

Figure 5. Evolution of mushy zone (a1–c1) and CAFÉ result (d1) in blade A; (a2–d2) in blade B; (a3–d3) in blade C. Blade A, B, and C corresponding to the samples solidified under 3mm/min, 8 mm/min and variable withdrawal rate, respectively.

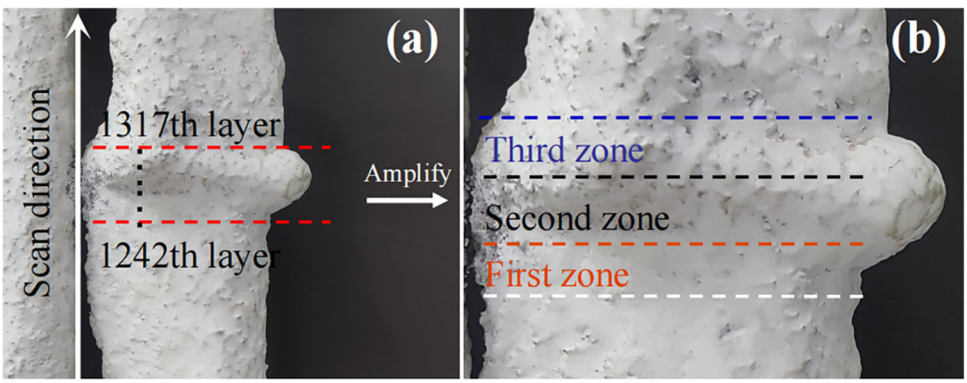

Figure 6. Schematic of the area of CT detection, (a) slice and scan direction; (b) upper and lower area of the edge plate.

Table 4. Measurement Zones of the Edge Plate

First zone	Second zone	Third zone
1242th layer	1256th layer	1278th layer
1247th layer	1265th layer	1290th layer
1252th layer	1273th layer	1317th layer

Figure 3 gives the CT apparatus, which mainly includes parts such as a Y.TU 450-D02 X-ray source from Yxlon, a PaxScan 2520 flat panel X-ray detector from Varian, and a rotating stage. During detection, the X-ray source was controlled by the computer system to emit X-rays and then, projected on the measured mold shell. The rotating stage drove the mold shell to rotate once, and 720 projection maps were formed on the flat detector which were then transmitted to the computer system for three-dimensional reconstruction. By using the artifact suppression technique proposed by Yang et al.[30], the reconstructed cross-section slices or 3D model showed good quality and clear structure. Considering the height of the mold shell, 2048 layers were set with a pixel size of 0.1mm, resulting in a total reconstructed length of 204mm. Then, Image J software was used to analyze the obtained slice images.

Results and Discussion

Effect of Withdrawal Rate on Stray Grain

Figure 4a–c presents the macrostructures of the three blades solidified under three strategies of withdrawal rate, and Figure 4d is the variable withdrawal rate curve of the third strategy. It could be seen that stray grain occurred at

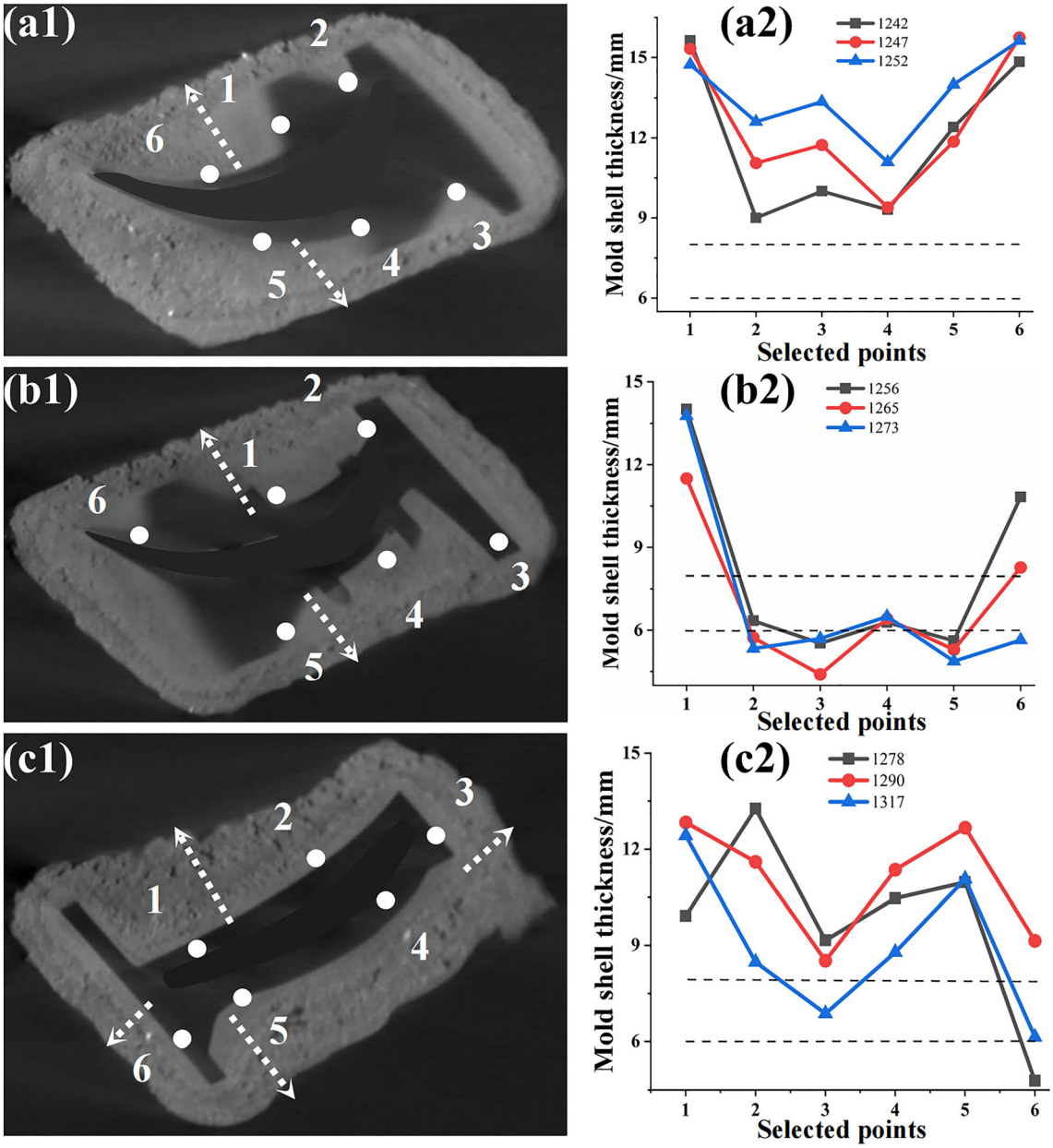

Figure 7. Schematic diagram of the position of selected points for counting the mold shell thickness: (a1) first zone; (b1) second zone; (c1) third zone; The thickness distribution curve of the corresponding point, (a2) first zone; (b2) second zone; (c2) third zone;

the edge plate of the three blades, and there is a significant contrast difference on both sides of the grain boundary. These experimental results indicated that the effect of decreasing or variable withdrawal rate on inhibition of the stray grain is limited.

To clarify the effect of the withdrawal rate on the stray grain of Figure 3, the evolution of the mushy zone adjacent to the edge plate and CAFÉ results of the edge plate in three blades were simulated, as shown in Figure 5.

Figure 5a1 demonstrates that the mushy zone on the trailing edge is higher than the leading edge at 3200s. As the solidification progresses to 3300s in Figure 5b1, the liquidus isotherm advances to the edge plate position, which is 10mm higher than the lowest liquidus isotherm of the blade body. Then, an isolated solid phase known as stray grain nucleation, occurred at the sharp corner when the liquidus isotherm moved to the edge plate, as shown in Figure 5c1. Since the melt and mold mainly dissipate heat in the form of radiation during the later stage of solidification, the thinner area (trailing edge) cools faster than the thicker area (leading edge), resulting in tilt of the liquidus isotherm and mushy zone.[5] As a result, an isolated undercooling region formed at the highest position of the liquidus isotherm, a new nucleus generated when the

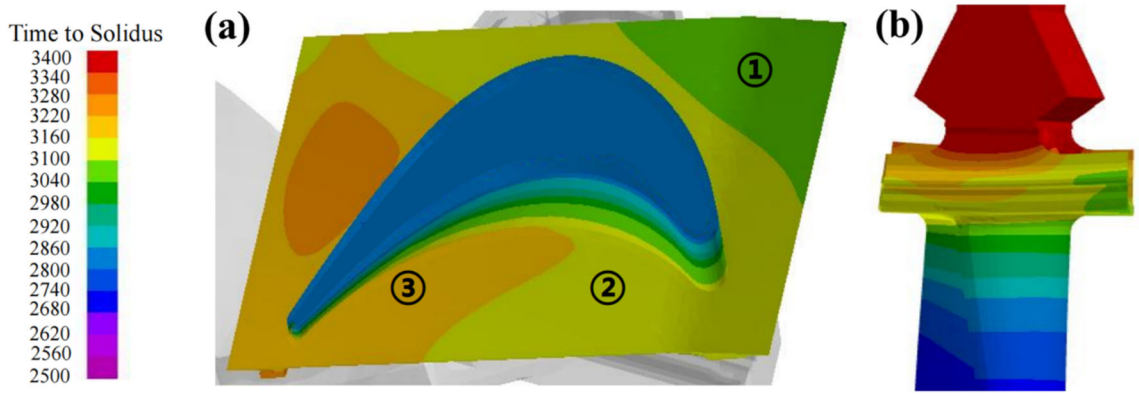

Figure 8. Solidification time of the edge plate of blade A, (a) top view; (b) front view.

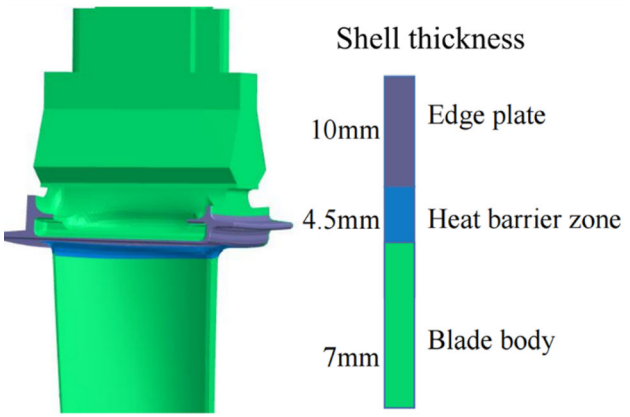

Figure 9. Schematic diagram of thickness distribution of non-uniform mold shell.

critical undercooling degree is reached, and then developed into a stray grain.[31] However, liquidus isotherm with irregular concave shape usually produces several stray grains,[32] such as two stray grains with different orientations from the primary SX shown by CAFÉ result in Figure 5d1.

Comparison between Figure 5a2, a1 reveals that the curvature of the mushy zone increases with an increase in withdrawal rate. This broadens the distance between the isolated undercooling region and the liquidus isotherm of the blade body to 20mm, as presented in Figure 5b2. This confirms the conclusion of Franke et al.[33] that the increase in withdrawal rate leads to the delay of heat loss of the solidified part, which intensifies the temperature difference between the inside and outside of the blade. The heat barrier zone is more prone to forming under high withdrawal rate conditions, which is consistent with the results of Ma[11]. Then, the number of produced stray grains increases, and the area is larger than the stray grains in Figure 5d2. Figure 5a3 demonstrates that the mushy zone is more stable under the widely used variable withdrawal rate, but the effect of inhibiting the production of the isolated undercooling region is still limited, as shown in Figure 5b3. And then it is still hard to prepare stray grain-free SX on some type of blade, as indicated in Figure 5d3.

These above simulation results confirm the experimental phenomenon well and cooperatively prove that modifying the withdrawal rate alone is insufficient to meet the demands of SX preparation. Due to the complex thermal conditions near the platform, it is necessary to adopt a variety of methods to suppress the stray grain formation.

Effect of Mold Shell Thickness on Stray Grain

Usually, the uniform thickness of mold shell in production is required to be 7mm, and a fluctuation of 1mm is considered allowed. Due to the complex structure of the edge plate, a cross-sectional analysis was performed at each structural mutation. Based on the distinct structural features and measurement points, the edge plate was divided into three zones, as illustrated in Figure 6. Among the 2048 layer slices, the 1242th layer through 1317th layer are located near the edge plate, and three slices were selected in each zone for investigating the mold shell thickness, as listed in Table 4.

Figure 7 demonstrates the CT images of the 1247th, 1265th, and 1290th layers, respectively, and the position of selected points for counting the mold shell thickness in the corresponding images. As shown in Figure 7a1, for the first zone (the transition region between the blade body and the edge plate), the statistical result in Figure 7a2 shows that the thickness of the mold shell seriously exceeds the specified tolerance. The short side of the edge plate near the trailing edge is thicker than the long side of the edge plate, which is in agreement with the results in Figure 5c1–c3. For the second zone, the thickness of areas such as points 2-5 is relatively thin and falls below the specified tolerance as shown in Figure 7b2, which confirms the conclusion that the cooling rate at the sharp corner of the edge plate is larger, and it is easy to form stray grain. For the third zone, the distribution of thickness is similar to that of the first region with most area exceeding 8mm, as indicated in Figure 7c2.

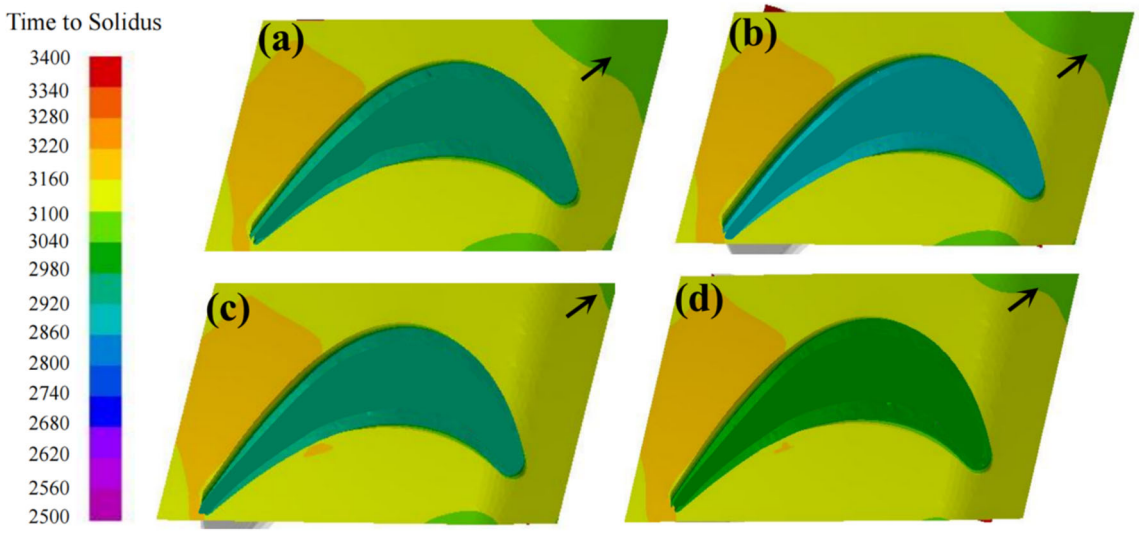

Figure 10. Solidification time of the edge plate with different mold shell thicknesses, (a) 8mm; (b) 9mm; (c) 10mm; (d) 11mm.

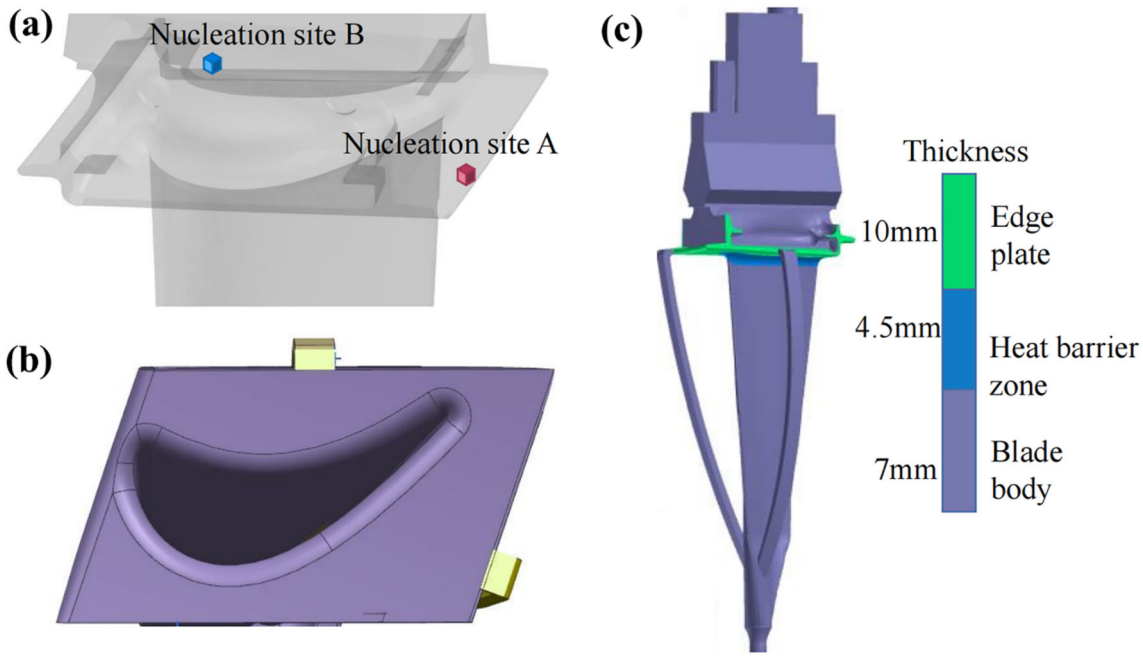

Figure 11. Schematic diagram of the combined control method, (a) nucleation site at the edge plate; (b) adding position of process bars; (c) non-uniform thickness of the mold shell.

As a result, the cooling rate in each area of the edge plate is inconsistent. Then, the solidification time of the edge plate of blade A was simulated, as illustrated in Figure 8. It could be seen that the edge plate can be nearly divided into three regions, i.e., regions 1, 2, and 3 corresponded to green, yellow and orange color, respectively. The root of the blade body was shown yellow and green. The solidification time of Region 1 is 120s earlier than that of Region 2, and that of Region 2 is 60s earlier than Region 3. Thus, it could be concluded that the thickness distribution of the mold shell under the edge plate exceeds the specified tolerance of 8mm, resulting in the formation of the heat barrier zone, which causes the edge plate to solidify first and consistent with the results in Figures 4a and 5b1.

Combined Control Method for Stray Grain

Design of the Combined Control Method

Strategy of Mold Shell with Non-uniform Thickness

In Section "Results and Discussion," it was deduced that the efficacy of modifying process parameters based on

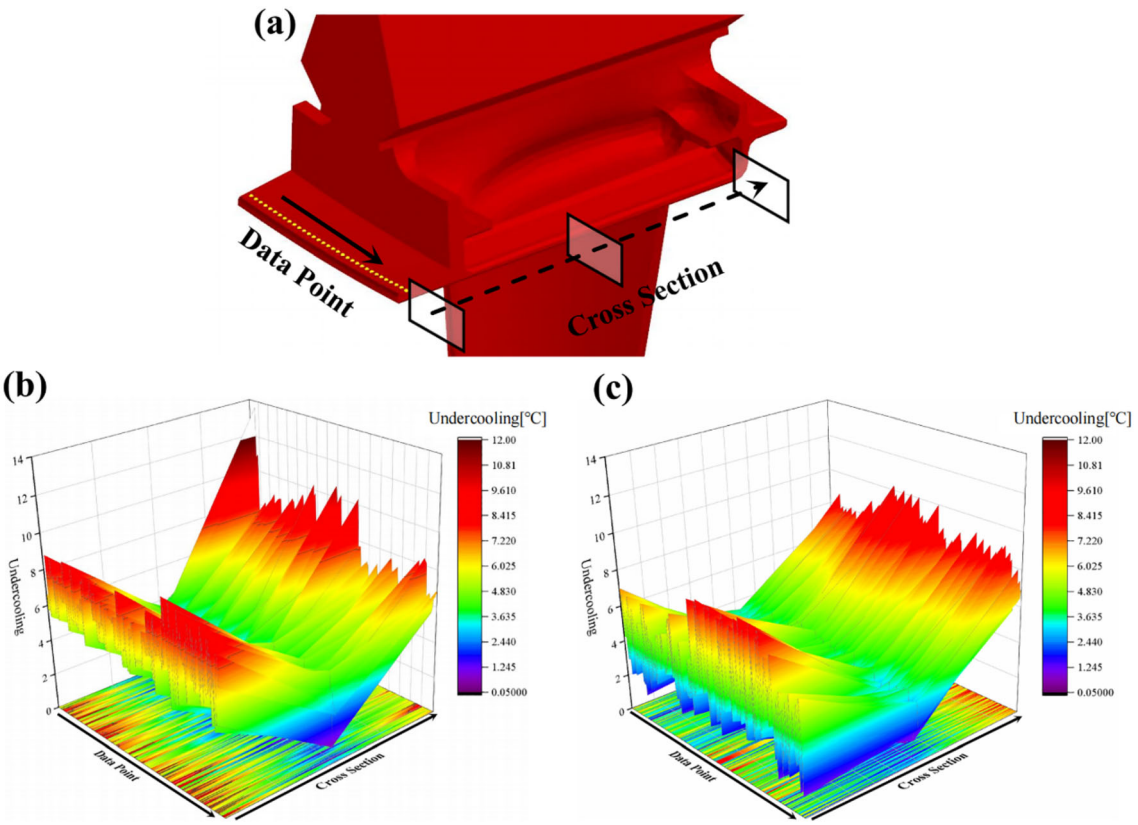

Figure 12. (a) Schematic diagram of the data point selection for count undercooling; (b) The undercooling before the method application; (c) The undercooling after the method application.

Table 5. Statistics of Undercooling

Undercooling [°C]	Range	Average
Before application	13.85	6.8
After application	7.56	4.65

uniform mold thickness to suppress stray grains is limited. The results of Qin et al.[9] confirmed that the non-uniform thickness of the mold shell has a certain effect on the suppression of defects. So, in this section, the non-uniform distribution strategy of mold shell thickness near the edge plate of the actual blade is discussed. According to Jia et al.,[34] if the dendrite in the blade body grows into the edge plate before the critical nucleation undercooling is reached at the edge plate, the formation of the stray grains will be suppressed. So, there are two methods to achieve this purpose, one is to increase the cooling rate of the heat barrier zone and another is to decrease the cooling rate of the undercooling region.

On the premise of ensuring the strength of the mold shell,[35] the thickness of the heat barrier zone marked with blue in Figure 9 was set firstly as 4.5mm. Then, the thickness of undercooling Region 1 was thickened to gain time for the growth of the dendrite in the blade body. Several thicknesses such as 8mm, 9mm, 10mm, and 11mm were successively adopted. Then, the cooling rate of Region 1 was assessed by simulation, as indicated in Figure 10. It is clear that the green area of Region 1 decreases first and then increases with continuous thickening of the corresponding region of the mold shell, and it almost disappears at a thickness of 10mm. Finally, a non-uniform distribution strategy of mold shell thickness is proposed, that is, 10mm in the edge plate, 4.5mm in the heat barrier zone, and 7mm in the remaining blade body.

Strategy of Process Bar Addition

Based on the aforementioned findings, a novel method for combined control of stray grains is proposed, which involves the following steps: (1) simulating the blade without process bars to determine the nucleation position at the edge plate, as illustrated in Figure 11a; (2) connecting the upper end of the process bar near the nucleation position and the lower end in the crystallization zone, as depicted in Figure 11b; (3) thickening the mold shell of the edge plate and reducing the thickness of the mold shell at the transition zone between the edge plate and the blade body, as shown in Figure 11c; (4) adopting a variable withdrawal rate as shown in Figure 4d.

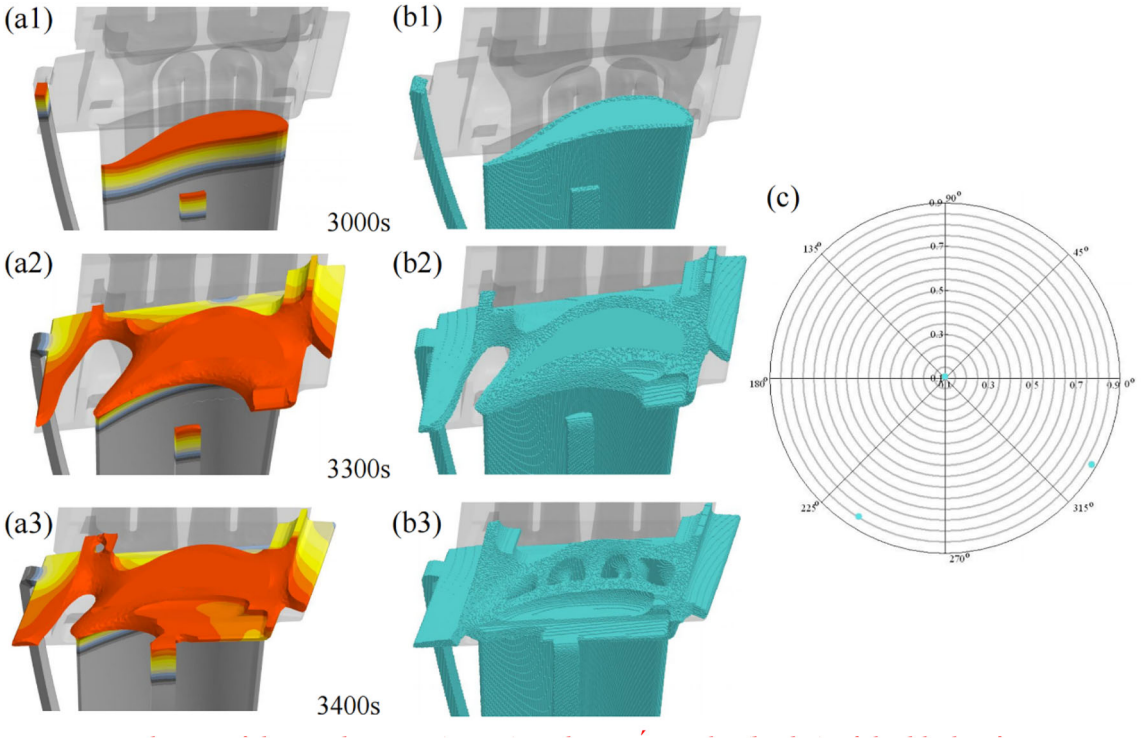

Figure 13. Evolution of the mushy zone (a1–a3) and CAFÉ results (b1–b3) of the blade after using the combined control method; (c) the <001> pole figure corresponding to the figure (b3).

The undercooling of the edge plate before and after implementing this method was counted. As shown in Figure 12a, three cross-sections were selected along the long edge of the edge plate, and 300 points in every section were selected for undercooling statistics. Then, the undercooling before and after implementing this method was presented in Figure 12b, c, respectively. An enhanced uniformity in the distribution of undercooling at the edge plate was observed in Figure 12c. The range of undercooling decreased significantly from 13.85 to 7.56, reflecting a reduction of 45.4%. Furthermore, the average undercooling exhibited a decrease from 6.8 to 4.65 °C, representing a substantial reduction of 31.6%, as shown in Table 5. Hence, a preliminary conclusion can be drawn that this method has a great effect on reducing the undercooling of the edge plate.

Application of the Combined Control Method for Stray Grain

Simulations were employed to analyze the effectiveness of the combined control method first. The evolution of the mushy zone and CAFÉ results adjacent to the edge plate after using the combined control method is shown in Figure 13. It can be observed from Figure 13a1 that the flat mushy zone is obtained both in the blade body and process bars. And the corresponding SX orientation is completely consistent, as shown in Figure 13b1. As the solidification progresses to 3300s in Figure 13a2, the mushy zone in the left process bar approaches the edge plate and bridges with the mushy zone in the platform. The overheating state of the heat barrier zone and the undercooling state of the edge plate are mitigated, which prevents the formation of the isolated solid phase. Then, the mushy zone of the platform part extends to the process bar position as shown in Figure 13a3; finally, the grain in the edge plate and the grain in the blade body converge to form an SX, as can be seen in Figure 13b3. The pole figure in Figure13c indicates that there is only a single grain on the edge plate, with a deviation from the <001> orientation of around 10°. This result further rules out the occurrence of stray grains, demonstrating the effectiveness of this method. These results provide evidence for experimental verification of the effectiveness of this method.

Then, a group of blades was cast by using this method to verify the effectiveness, and the images of the blade after macro etched were given in Figure14. It is showed that the surface of the blade maintains well SX integrity, and stray grains in Figure 4 were successfully suppressed. Moreover, it should be noted that the process bar shows with curved rather than straight shape, which is different from the results in Meyer et al.[12] this shape was designed to prevent cracks at the edge plate that are caused by excessive solidification stress.[36] Research on the shape selection of the process bar will be reported in the future.

It is necessary to confirm whether there are stray grains in the focused edge plate. As indicated by macrostructures in

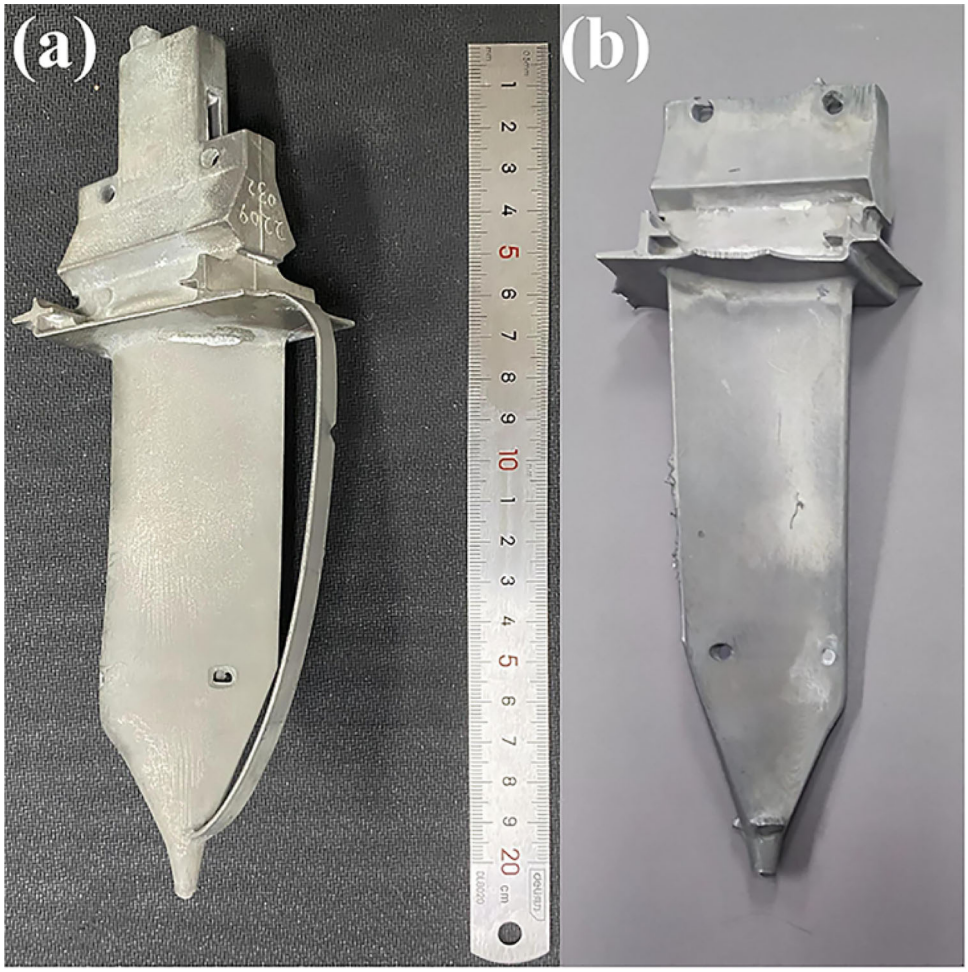

Figure 14. Blade cast by the combined control method, (a) before removing process bars; (b) after removing process bars.

Figure 15a1, b1, the uniform contrast means no stray grains are at the entire platform and edge plate. Figure 15c1 is the position of the blade body under the platform, whereas the microstructure is shown in Figure 14c2 exhibited with a cruciform dendrite.

Microstructures in Figure 15a2, b2 demonstrate that a strong secondary dendrite arm occupied the edge plate, which propagated from the primary dendrite in Figure 15c2. The above dendrite microstructures are consistent with the results of Ren et al.[8] Thus, it can be concluded that the experimental results of this method are in well coincide with the simulation results, which further verified the effect of inhibiting stray grains.

Conclusion

In this study, the temperature field and the solidified grain structure of a single crystal blade were simulated by using the macro-scale section of the commercial modeling code and mesoscale CAFÉ model, respectively. Combined with industrial cone-beam CT detection and a directional solidification experiment, an effective combined control method for stray grain was proposed. The major conclusions of this work can be summarized as follows:

1. The evolution of the mushy zone and the growth of grain simulated by the temperature field and CAFÉ model illustrated that the effectiveness of decreasing or variable withdrawal rate is limited and cannot meet the manufacturing requirement of the complex structure SX blade without stray grain.
2. The thickness distribution of the mold shell adjacent to the edge plate was quantified by an industrial cone-beam CT system, and the formation reason of the heat barrier zone was verified. Based on this, a non-uniform distribution strategy of mold shell thickness was designed, that is, 10mm in the edge plate, 4.5mm in the heat barrier zone, and 7mm in the remaining blade body.
3. A combined control method was proposed, which incorporated a process bar, non-uniform mold shell, and variable withdrawal rate. Notably, the undercooling range and average undercooling of the edge plate exhibited a significant decrease

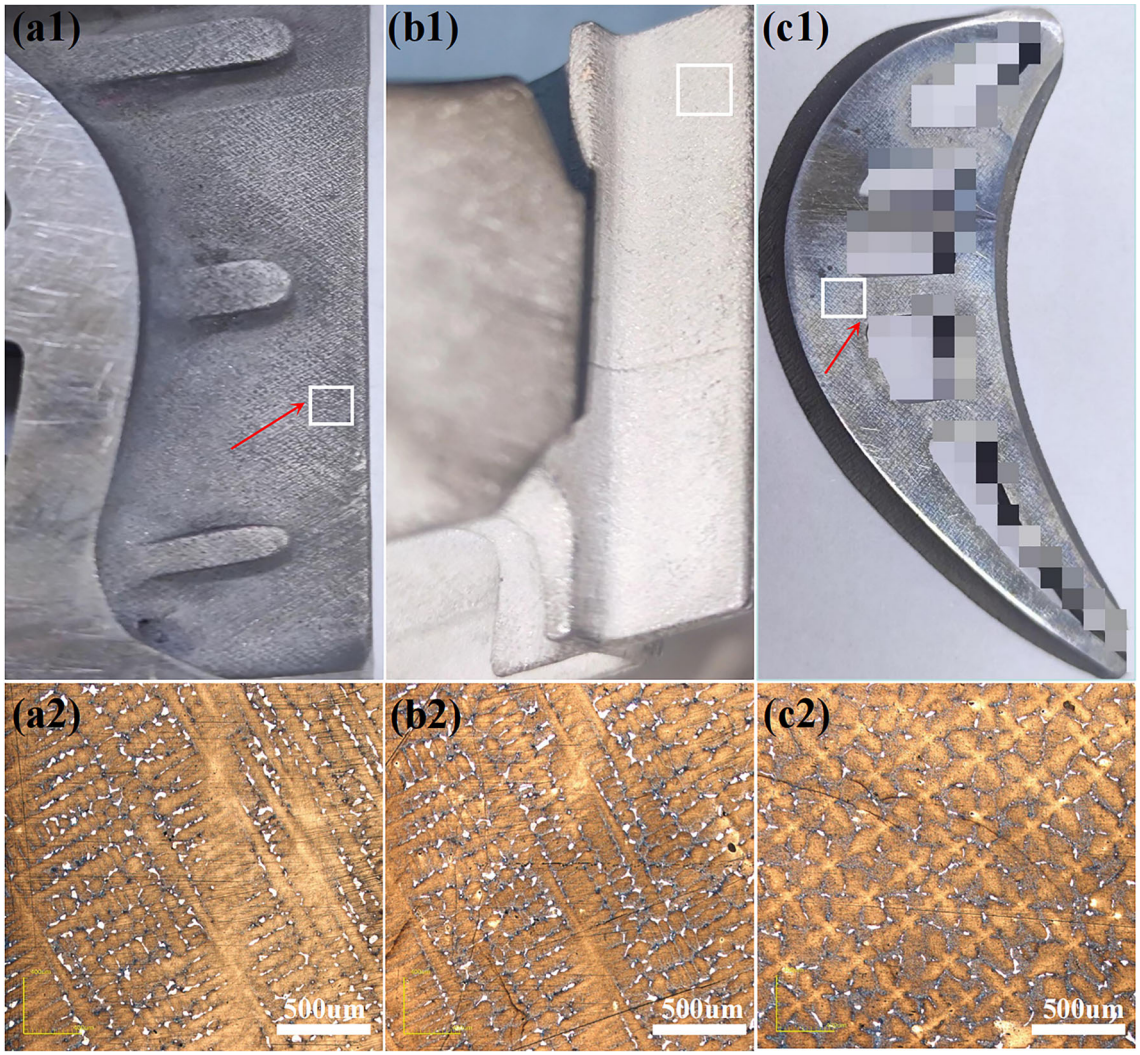

Figure 15. The macrostructure of different positions of the blade, (a1) edge plate; (b1) platform; (c1) blade body. (a2–c2) are the microstructures of the corresponding white-framed region in figure (a1–c1).

from 13.85 to 7.56, and 6.8 to 4.65, respectively. Simulation and experiment results have proven highly effective of this method in suppressing the formation of stray grains of SX blades.

Acknowledgements

This work was sponsored by National Science and Technology Major Project (J2019-VII-0013-0153) and Postdoctoral Fellowship Program of CPSF (GZC20233515).

REFERENCES

1. G. Gudivada, A.K. Pandey, Recent developments in nickel-based superalloys for gas turbine applications: Review. J. Alloys Compd. **963**, 14 (2023)
2. Y.F. He, S.G. Wang, J. Shen, D. Wang, Y.Z. Lu, L.H. Lou, J. Zhang, Evolution of micro-pores in a single crystal nickel-based superalloy during 980 °C creep. Acta Metall. Sin.-Engl. Lett. **35**(8), 1397–1406 (2022)
3. B.Q. Wang, L. Zeng, M.X. Xia, N. Ren, J.G. Li, Substrate stimulating technique for ni-based single crystal superalloy preparation during direction solidification. Mater. Des. **224**, 9 (2022)
4. M. Huo, C.Y. Chen, H.Y. Jian, W.C. Yang, L. Liu, M. Motyka, C.Y. Jo, The stray grains from fragments in the rejoined platforms of ni-based single-crystal superalloy. Metals. **13**(8), 10 (2023)
5. D. Szeliga, Eliminating equiaxed grain defects in a ni-based single-crystal blade platform by flattening the liquidus isotherm. Adv. Eng. Mater. **13** (2023)
6. W. Tan, X. Xue, T. Yu, W. Li, P. Yan, Q. Zeng, Formation mechanism of stray grain in the transition zone between airfoil and platform of nickel-based single crystal blade. Rare Met. Mater. Eng. **51**(4), 1348–1355 (2022)
7. Z. Shang, H.J. Niu, X.P. Wei, D.Z. Song, J.T. Zou, G. Liu, S.H. Liang, L.P. Nie, X.F. Gong, Microstructure

and tensile behavior of nickel-based single crystal superalloys with different Re contents. J. Mater. Res. Technol. JMRT **18**, 2458–2469 (2022)
8. N. Ren, J. Li, B.Q. Wang, L. Zeng, M.X. Xia, J.G. Li, Design of variable withdrawal rate for superalloy single-crystal blade fabrication. Mater. Des. **198**, (2021)
9. L. Qin, J. Shen, G.X. Yang, Q.D. Li, Z. Shang, A design of non-uniform thickness mould for controlling temperature gradient and S/L interface shape in directionally solidified superalloy blade. Mater. Des. **116**, 565–576 (2017)
10. D. Szeliga, K. Kubiak, J. Sieniawski, Control of liquidus isotherm shape during solidification of Ni-based superalloy of single crystal platforms. J. Mater. Process. Tech. **234**, 18–26 (2016)
11. D.X. Ma, Development of single crystal solidification technology for production of superalloy turbine blades. Acta Metall. Sin. **51**(10), 1179–1190 (2015)
12. M. Meyer, D. Dedecke, U. Paul, S. Kwu, Undercooling related casting defects in single crystal turbine blades. Superalloys 471–479 (1996)
13. F. Qiu, K. Bu, B.J. Zheng, G.L. Tian, Control of edge plate stray grain of single-crystal turbine blade by using process bar method. Int. J. Metalcast. **14**(1), 144–154 (2020). https://doi.org/10.1007/s40962-019-00338-9
14. S.J. Ren, K. Bu, S. Mou, R.Y. Zhang, B.X. Bai, Control of dimensional accuracy of hollow turbine blades during investment casting. J. Manuf. Process. **99**, 548 (2023)
15. M.Z. Xu, S.N. Lekakh, V.L. Richards, Thermal property database for investment casting shells. Int. J. Metalcast. **10**(3), 329–337 (2016). https://doi.org/10.1007/s40962-016-0052-4
16. X. Liu, Y. Wang, H. Zheng, Z. Guo, G.H. Liu, Z.D. Wang, Investigation and application of inverse determination of interfacial heat transfer coefficient in vacuum investment casting. Int. J. Metalcast. (2024). https://doi.org/10.1007/s40962-023-01240-1
17. S. Mou, K. Bu, S.J. Ren, J. Liu, H.Y. Zhao, Z.X. Li, Digital twin modeling for stress prediction of single-crystal turbine blades based on graph convolutional network. J. Manuf. Process. **116**, 210–223 (2024)
18. M.S. Varfolomeev, G.I. Shcherbakova, Interaction of a ceramic casting mold material of the Al_2O_3–Al_2O_3 composition with a nickel-based superalloy. Int. J. Metalcast. **15**(4), 1309–1316 (2021)
19. F. Qiu, K. Bu, J.H. Song, G.L. Tian, X.D. Zhang, Dimensional control of nickel-based single crystal turbine blade investment casting by process control optimization. Int. J. Metalcast. **12**(3), 469–479 (2018)
20. X. Guo, A.T. Yang, D.Y. Zhao, J. He, F. Tao, Q.Y. Zhang, Z.H. Yang, Research on displacement and wall thickness evolution of gas turbine blade during casting process based on cantilever structure core. J. Chin. Soc. Power Eng. **41**(6), 452–459 (2021)
21. J.X. Wu, Y.Y. Chen, Z.M. Du, H.Y. Jiang, Modeling of investment casting of Ti48Al48Cr2Nb2 (at%) alloy air rudder skeleton. Int. J. Metalcast. **17**(3), 2002–2016 (2023). https://doi.org/10.1007/s40962-022-00907-5
22. C.A. Gandin, M. Rappaz, D. West, B.L. Adams, Grain texture evolution during the columnar growth of dendritic alloys. Metall. Mater. Trans. A **26**(6), 1543–1551 (1995)
23. C.A. Gandin, J.L. Desbiolles, M. Rappaz, P. Thevoz, A three-dimensional cellular automation-finite element model for the prediction of solidification grain structures. Metall. Mater. Trans. A **30**(12), 3153–3165 (1999)
24. A. Kermanpur, N. Varahram, P. Davami, M. Rappaz, Thermal and grain-structure simulation in a land-based turbine blade directionally solidified with the liquid metal cooling process. Metall. Mater. Trans. B **31**(6), 1293–1304 (2000)
25. H.X. Xia, Y.H. Yang, Q.S. Feng, Q.Y. Xu, H.B. Dong, B.C. Liu, Generation mechanism and motion behavior of sliver defect in single crystal ni-based superalloy. J. Mater. Sci. Technol. **137**, 232–246 (2023)
26. W. Kurz, B. Giovanola, R. Trivedi, Theory of microstructural development during rapid solidification. Acta Metall. **34**(5), 823–830 (1986)
27. B.Q. Wang, L. Zeng, N. Ren, M.X. Xia, J.G. Li, A comprehensive understanding of grain selection in spiral grain selector during directional solidification. J. Mater. Sci. Technol. **102**, 204–212 (2022)
28. Z.F. Liu, K. Miao, W.B. Lian, Z.L. Lu, D.C. Li, Elimination of the stray grain defects of single crystal blade by variable wall thickness based on integral ceramic mold. Metals **12**(11), 11 (2022)
29. K. Cui, W.H. Wang, R.S. Jiang, D.Z. Zhao, A wall-thickness compensation strategy for wax pattern of hollow turbine blade. Chinese. J. Aeronaut. **32**(8), 1982–1993 (2019)
30. F.Q. Yang, D.H. Zhang, K.D. Huang, Y. Yang, Iterative excitation with noise rejection techniques for x-ray computed tomography of hollow turbine blades. Nondestruct. Test. Eva. **38**(1), 172–188 (2023)
31. D.X. Ma, Y.X. Zhao, W.T. Xu, F.Z. Xu, J.H. Wei, H.J. Zhang, Comparative investigation of the undercooling capacity and single-crystal castability of some ni-based superalloys. Crystals **13**(1), 11 (2023)
32. X.W. Yan, Q.Y. Xu, G.Q. Tian, Q.W. Liu, J.X. Hou, B.C. Liu, Multi-scale modeling of liquid-metal cooling directional solidification and solidification behavior of nickel-based superalloy casting. J. Mater. Sci. Technol. **67**, 36–49 (2021)
33. M.M. Franke, R.M. Hilbinger, A. Lohmuller, R.F. Singer, The effect of liquid metal cooling on thermal gradients in directional solidification of superalloys: Thermal analysis. J. Mater. Process. Tech. **213**(12), 2081–2088 (2013)

34. Y.L. Jia, L.L. He, Y.S. Zhao, H.M. Guo, X. Fang, J. Zhang, Determination of undercooling time for stray grain formation of dd11 single crystal superalloy. J. Aeronaut. Mater. **35**(4), 8–15 (2015)
35. H. Jafari, M.H. Idris, A. Ourdjini, Effect of thickness and permeability of ceramic shell mould on in-situ melted AZ91D investment casting. Appl. Mech. Mater. **465**, 1087 (2013)
36. A. Wall, M.J. Benoit, A review of existing solidification crack tests and analysis of their transferability to additive manufacturing. J. Mater. Process. Tech. **320**, 118090 (2023)